OPTOELECTRONICS AND ADVANCED MATERIALS – RAPID COMMUNICATIONS Vol. 1, No. 10, October 2007, p. 510 - 519

Electrical and electromechanical studies on tungsten-bronze electroceramic: lead potassium dysprosium niobate

K. SAMBASIVA RAO*, D. MADHAVA PRASAD, P. MURALI KRISHNA, T. SWARNA LATHA, JOON HYUNG LEE[a]

Centre for Piezoelectric Transducer Materials, Department of Physics, Andhra University, Visakhapatnam – 530 003, India

[a]*Department of Inorganic Materials Engineering, Kyungpook National University, Daegu, 702701, Korea*

Lead potassium dysprosium niobate (PKDN) has been prepared by a standard conventional ceramic route. Material formation has been confirmed by X-ray diffraction (XRD) studies. The variation of dielectric constant with temperature is explained considering the space-charge polarization. Complex impedance spectroscopy (CIS) analysis has been carried out to investigate its electrical properties as a function of frequency and temperature. CIS analysis has indicated the electrical behavior of the material sample shows negative temperature coefficient of resistance (NTCR) typical to a semiconductor behavior. Impedance studies indicated the presence of temperature dependant relaxation process in the material with a spread of relaxation time. Modulus analysis reveals the possibility of hopping mechanism for electrical processes in the system. The frequency dependant ac conductivity at different temperatures showed the conduction process is thermally activated process.

(Received August 16, 2007; accepted August 30, 2007)

Keywords: Ceramics, Solid-state reaction, X-ray diffraction, Ferroelectric, Piezoelectric, Impedance, Electric modulus, Conductivity

1. Introduction

The oxygen-octahedra ferroelectrics have a number of useful properties for optical and ultrasonic device applications. This class of materials includes a number of ferroelectric oxides, i.e., the pervoskite, tungsten-bronze (TB), pyrochlore and $LiNbO_3$-type structures.

Lead Potassium Niobate crystal ($Pb_2KNb_5O_{15}$, PKN) with a TB structure is attracting from the viewpoints of nonlinear optics and piezoelectric applications. Dielectric, optical, elastic and piezoelectric properties [1, 2] were reported in PKN. Furthermore, a possibility for surface acoustic wave (SAW) devices was investigated [3].

Ceramic samples with general formula $Pb_{1-x}K_{2x}Nb_2O_6$ (PKN) have been processed with different values of x. PKN with x = 0.20, is the useful material for high speed broad band surface acoustic wave devices. Impedance spectroscopy, electric modulus spectroscopy and AC conductivity studies on ceramics of PKN with x = 0.20, 0.26 and 0.29 have been reported by Rao et al. [4-6].

Impedance spectroscopy (IS) has been widely used for analyzing the electrical relaxation in ionic conductors [7-9] and conducting glasses [10-12]. Amongst ferroelectric materials many a.c complex impedance investigations have been done on semiconducting BaTiO3 [13, 14] and ion conducting $LaTaO_3$ [15, 16]. Much less attention paid to other ferroelectric materials, the reason being probably that a ferroelectric compound is usually a good insulator. Analysis of IS provides an opportunity to separate out grain and grain boundary capacitive effects, which are prevalent in ferroelectric ceramics and using the data is also possible to calculate the relaxation times (τ) [17].

Literature showed, no work has been published concerning the dielectric and the temperature and frequency dependent electrical properties of ceramics on Dysprosium modified PKN with x = 0.29. In an effort to investigate the physical properties, we have undertaken systematic measurements by x-ray diffraction, dielectric permittivity, impedance spectroscopy, Ac and Dc conductivity.

2. Synthesis and characterization

$Pb_{0.71}K_{0.145}Dy_{0.145}Nb_2O_6$ (PKDN) has been prepared by using the following chemical reaction

$$0.71(PbO) + 0.0725(K_2CO_3) + 0.0725(Dy_2O_3) + Nb_2O_5 \rightarrow Pb_{0.71}K_{0.145}Dy_{0.145}Nb_2O_6 + 0.0725CO_2 \quad (1)$$

Analar grade oxides and carbonates are taken and thoroughly mixed for 6 hrs and calcinated at 900 ^oC for 4 hrs. The calcination process has been repeated thrice with intermediate grinding. The mixture has been grounded; polyvinyl alcohol has been added as binder and pressed into disc form using hydraulic press at 580 MPa. The green bodies obtained have been sintered at 1220 ^OC for 60 min.

The calcined powder has been examined by x-ray diffraction (XRD) using Phillips X'pert diffractometer with Cu K_α radiation. For the dielectric, impedance and conductivity studies the pellet surfaces have been polished

and electroded with silver paste. The capacitance, dielectric loss, impedance and conductivity have been measured as a function of temperature; from 35 ^{o}C to 590 ^{O}C at selected frequencies between 45 Hz to 5 M Hz using computer controlled HIOKI 3532-50 LCR Hitester.

3. Results and discussion

XRD

Fig. 1 shows the x-ray diffraction pattern of the sample taken at room temperature. The preparation procedures employed resulted in single phase material with orthorhombic structure. The lattice parameters were estimated using Interpretation and Indexing program by E. Wu, School of physical Sciences, Flinders University of South Australia, Bed ford park, Australia [18]. The lattice parameters of $Pb_{0.71}K_{0.145}Dy_{0.145}Nb_2O_6$ (PKDN) are found to be a = 17.5512 Å, b = 18.1292 Å and c = 3.8680 Å. The unit cell shrinks with the Dy^{3+} substitution when compared with PKN [6]. The density about 98.8% to that of theoretical value obtained indicating the material has been sintered well. Lattice parameters, orthorhombic distortion, cell volume, theoretical density ($d_{X\text{-}Ray}$), experimental density (d_{expt}), porosity and % density values are given in the Table1.

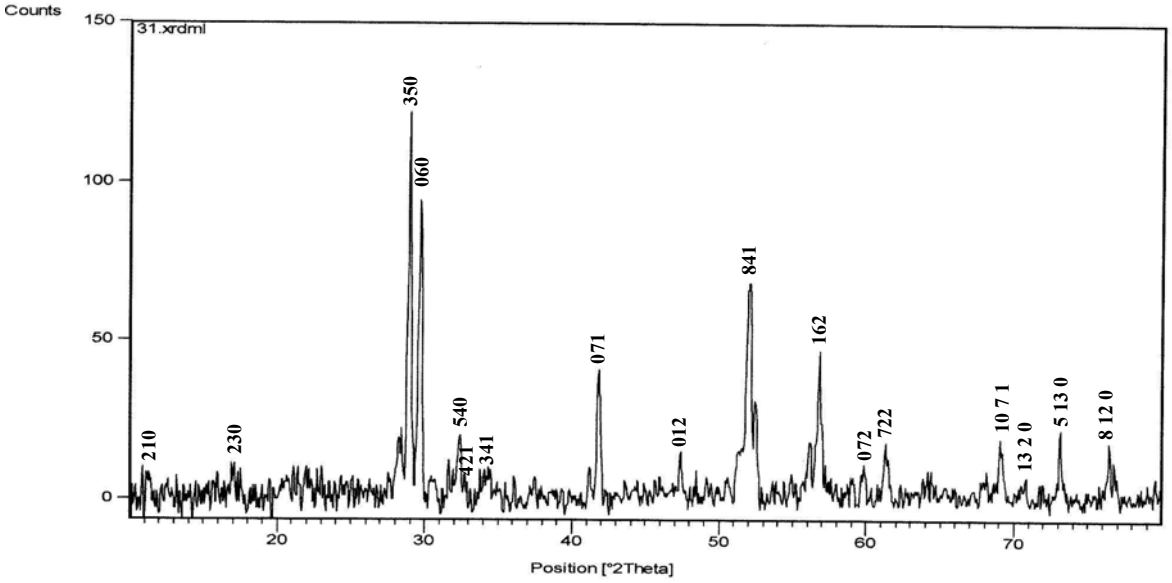

Fig. 1. The x-ray diffractogram of PKDN.

Table 1. Lattice parameters of PKDN.

Composition	Lattice parameters (Å)	Orthorhombic distortion (b/a)	Density (g/cm^3) X-Ray	Expt	Porosity	% density
PKDN	a = 17.5512 b = 18.1292 c = 3.8680	1.03	6.16	6.06	0.012	98.8

Hysteresis

The sample has been poled by applying 1.5 kV/mm at 125 ^{o}C for 30 min. by field-cooled method [19]. The temperature at which the sample ahs been poled is less than the Curie temperature of the composition. The behavior of the ferroelectric material can be understood in terms of hysteresis loop. Fig. 2 shows the hysteresis loop of PKDN. The hysteresis appears in the ferroelectrics because of the motion of the domain walls in the ferroelectric material. If an external electric field is applied then the domain favorably oriented with respect to the field and the wall motion grows at the expense of other less favorably oriented. The values of room temperature spontaneous polarization (P_s), remenant polarization (P_r) and coercive field (E_c) obtained on the material are given in the Table 2.

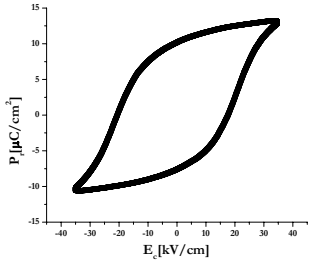

Fig. 2. Hysteresis loop.

Table 2. Hysteresis parameters.

P_r (μC/cm^2)	13.5
P_s (μC/cm^2)	10.5
E_c (kV/cm)	20

Dielectric

Fig. 3 shows the temperature dependence of real dielectric constant (ε') for PKDN ceramic at different frequencies. At 0.5 KHz, 1 KHz, 10 KHz and 20 KHz, the dielectric constant peak corresponding to the ferroelectric-paraelectric phase transition (T_C) can be well defined. The T_C has been observed at 200 ^oC. Further, no shift in T_C has been observed at different frequencies, revealing the material belongs to traditional ferroelectric. Inset of the Fig. 3 shows the temperature dependence of imaginary dielectric constant at 0.5 kHz and 1 kHz. From the inset of Fig. 3 it is clear that, a peak in the value of ε^{II} has been observed at a particular temperature, 200 ^oC. The temperature at which peak is observed is exactly coincides with the value of T_C. Curie's constant has been evaluated using Curie-Weiss law in the para region. The values of ε'_{RT}, ε'_{TC}, T_C and Curie constant have been given in Table 3.

Table 3. Dielectric data.

Composition	PKDN
ε^{I}_{RT} (1kHz)	2139
T_C ^oC	200
ε^{I}_{TC} (1KHz)	3761
Curie Constant, K (X 10^5)	1.2

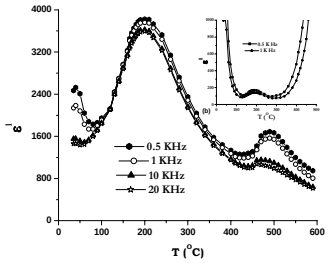

Fig. 3. Temperature dependence of dielectric constant at different frequencies. Inset: Temperature dependence of imaginary dielectric constant at 0.5 KHz and 1 KHz.

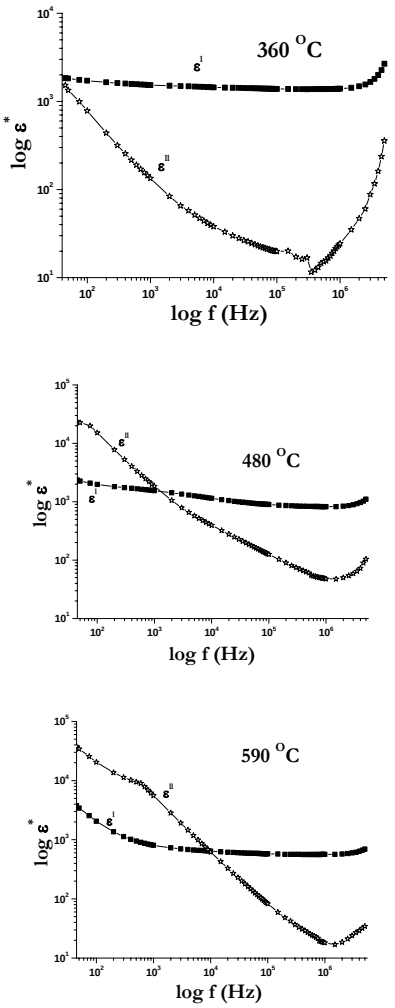

Fig. 4. Variation of real (ε') and imaginary (ε") parts of the dielectric constant as a function of frequency at different temperatures.

Fig. 4 shows the variation of real and imaginary parts of the dielectric constant, ε' and ε", as a function of frequency at various temperatures. Both ε' and ε" rise sharply towards low frequencies and the shape of rise is changed as increasing in temperature. The sharp rise of the real and imaginary part of dielectric constant at low frequency is due to most probably to the conducting ion motion [20]. When dealing with a charge carrier system in high-conducting material, it was preferable to plot the ac complex impedance or conductivity instead of the dielectric loss for characterizing ferroelectric materials [20].

As seen in Fig. 4, both the real and imaginary part of dielectric constant, ε' and ε", exhibit high value which reflect the effect of space charge polarization and/or conducting ionic motion. As it is known, in the conducting dielectric materials, high ε' values may be related to the accumulation of charges at the interface between the sample and electrodes, i.e., space charge polarization [20,

21]. Corresponding, ε" of the low frequency become very high due to free-charge motion within the material and are connected to ac conductivity relaxation. A further analysis of the dielectric behavior would be more successfully achieved by using the formulation of dielectric modulus spectroscopy which suppresses the effects of the electrode polarization or mobile ion polarization.

Frequency dependence of the dielectric constants ε' and ε"

The frequency dependence of ε' and ε" on a log–log scale at different temperatures are shown in Fig. 5 (a) and (b). Both ε' and ε" show strong dispersions at low frequencies. This event is attributed to the low frequency space charge accumulation effect. Such strong dispersions in both the components of the complex dielectric constant appear to be a common feature in ferroelectrics associated with non-negligible ionic conductivity and is referred to as the low frequency dielectric dispersion (LFDD) [22, 23]. Detailed studies of this phenomenon were carried by Jonscher et al. [24].

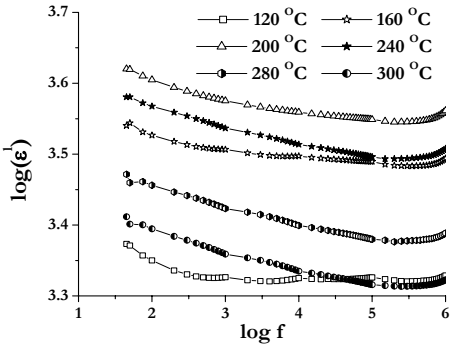

Fig. 5 (a). Frequency dependency of ε' on a log-log scale at different temperatures.

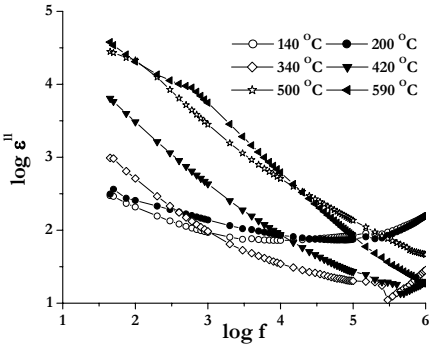

Fig. 5 (b). Frequency dependency of ε" on a log-log scale at various temperatures.

The dispersion in the imaginary part of the dielectric constant (ε") is stronger than that in the real part implying that it is influenced by dc conductivity. The low frequency slope of the curve log ε" vs. log f is close to -1 indicating the predominance of the dc conduction in this frequency region. Fig. 6 shows the variation of the real part of the ac conductivity as a function of frequency at a few elevated temperatures. It indicates the existence of low frequency independent plateau-like region [σ_{dc}] and subsequently the conductivity increases with increase in frequency, varying approximately as a power of frequency (ω^n) (where n is a function of temperature as well as frequency) at all the temperatures. However, the trend of the curve does not change with temperature; only the onset of the dispersion is shifted to higher frequencies as the temperature is increased. This observation is in line with that reported in the literature for $0.3Na_2O_{0.7}B_2O_3$ glass samples by Roling et al. [25].

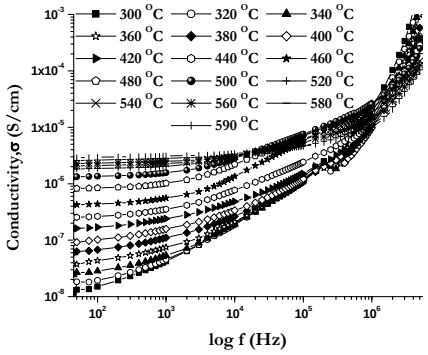

Fig. 6. AC conductivity vs frequency at several temperatures.

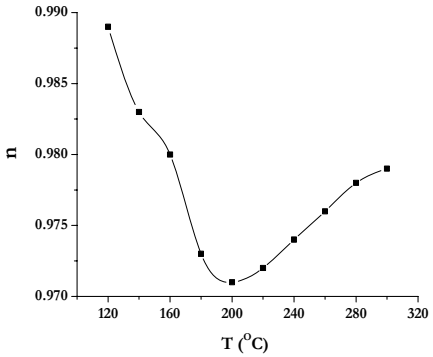

Fig. 7. Variation of critical exponent n (T) with temperature showing a minimum at T_C.

Fig. 7 shows the variation of critical exponent n(T) with temperature. The interaction between the charge carriers participating in the polarization process is characterized by the parameter n. A unit value of n implies a Debye case, and it is attainable [26] at very low temperatures. However, as the temperature increases, the interaction increases, leading to a decrease in n. The value of n calculated from the high frequency region decreases as the temperature increases and attains a minimum near T_c and subsequently it increases with further increase in temperature. The observed minimum at T_c implies the strong interaction between the charge carriers and the lattice.

Dielectric dispersion relations and interpretation of the experimental results

The complex dielectric constant as a function of the frequency ω in accordance with the Jonscher's power law.

$$\varepsilon^* = \varepsilon'-i\varepsilon'' = \varepsilon_\infty+\sigma/i\varepsilon_o\omega+(a(T)/\varepsilon_0)(i\omega^{n(T)-1}) \quad (2)$$

where ε_∞ is the 'high frequency' value of the dielectric constant, n(T) is the temperature-dependent exponent and a(T) determines the strength of the polarizability arising from the universal mechanism in question. The real and imaginary parts of the complex dielectric constant are given

$$\varepsilon' = \varepsilon_\infty+\mathrm{Sin}(n(T)\pi/2)\omega^{n(T)-1}\,(a(T)/\varepsilon_0) \quad (3)$$

$$\varepsilon'' = \sigma/\varepsilon_o\omega +\mathrm{Cos}(n(T)\pi/2)\omega^{n(T)-1}\,(a(T)/\varepsilon_0) \quad (4)$$

Where the first term in Eq. (3) determines the lattice response and that in the Eq. (4) corresponds to the dc conduction part, while the second term in both the equations reflects the charge carrier contribution to the dielectric constant. The temperature and frequency dependencies of the dielectric constant ε' (Figs. 3 and 5 (a)) could be explained by Eq. (3). The charge carrier term $(\mathrm{Sin}(n(T)\pi/2)\omega^{n(T)-1}\,(a(T)/\varepsilon_0))$ dominates at low frequency and ε_∞ is negligible. Therefore, for a constant n, Eq. (3) yields a straight line with a slope equal to n-1 in the double logarithmic plot of ε' and frequency. At high frequencies the charge carriers fail to respond to the external field, therefore the measured dielectric constant is due to the contribution from the lattice polarization. This accounts for a linear decrease in the low frequency region and a frequency-independent plateau region at high frequencies (Fig. 5 (a)). As A(T) (a(T)) increases with increase in temperature [27], the charge carrier term becomes more and more prominent at high temperatures, thereby resulting in the low frequency dielectric dispersion. An anomalously strong dispersion of ε' near T_c suggests the coupling between the charge carriers and the lattice [28]. The behavior of ε'' could be explained by Eq. (4). Careful analysis of Fig. 5 (b) indicates the existence of two slopes corresponding to -1 in the low frequency region and -(1-n) in the high frequency region. As the dc conductivity term increases with increase in temperature, the second term in Eq. (4) is totally over-shadowed by the first term. So at low frequencies and high temperatures, the dc conductivity term dominates and yields a slope of -1, which indeed is consistent with the data shown in Fig. 5 (b). Fig. 8 shows the temperature dependence of the prefactor A(T) showing a peak at T_C. The prefactor A(T) which determines the strength of polarizability exhibits a peak at T_C [22].

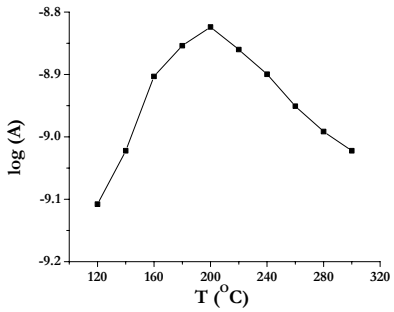

Fig. 8. The temperature dependence of the prefactor A(T) showing a peak at T_C.

Piezoelectric

Piezoelectric coefficients - electromechanical coupling factor (planar mode, K_p and thickness mode, K_t), electromechanical coupling factor (31 mode, K_{31}), piezoelectric charge constants (d_{31}, d_{33}, 10^{-12}C/N) and piezoelectric voltage constant (g_{33}, 10^{-3} mv/N) and stiffness constant (S_{11}^E) have been measured in PKDN composition poled at 135 ^{0}C for 30 min at 4 KV/mm by field cooled method. These values are given in table 4. The values of Kp = 0.27, K_t = 0.34, N_t = 1698, K_{31} = 0.19, d_{31} = -34, d_{33} = 85, g_{33} = 14.3 and S_{11}^E = 12.7 have been found in PKDN.

The electromechanical coupling constants are mostly dependent on synthesis and also particular dopent. The piezoelectric charge constant d33 = 85 X 10^{-12} C/N in PKDN which is much higher compared with some of the TB ferroelectrics [29, 30].

Table 4. Piezoelectric data of PKDN.

Composition	K_P	K_t	K_{31}	$S_{11}^E \times^{-12}$ m^2/N	$d_{31} \times 10^{-12}$ C/N	$d_{33} \times 10^{-12}$ C/N	$g_{33} \times 10^{-3}$ mV/N
PKDN	0.27	0.34	0.19	12.7	-34	85	14.3

Impedance spectroscopy

Polycrystalline materials contain grain and grain boundaries whose capacitive effects have profound effect on the ferroelectric properties. Alternating current impedance analysis is a powerful tool in separating out the grain and grain boundary effects [31]. In the complex impedance plots (Z' vs Z''), a single semicircle indicates grain effects, which can be shown as a combination of two parallel resistance-capacitance (RC) elements and the second semicircle indicates the presence of grain boundary effects. If a third, is present, it indicates the electrode

effects. Each semicircle, which is made up of a parallel combination of RC, are interconnected serially [31].

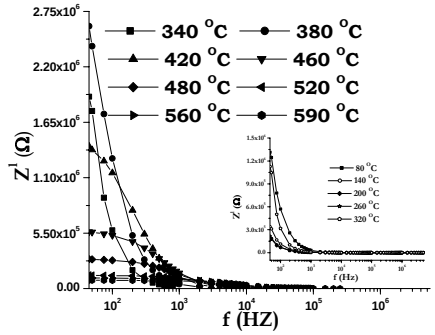

Fig. 9 Variation of real part of impedance (Z') with frequency at various temperatures. Inset: Variation of real part of impedance upto 320 °C.

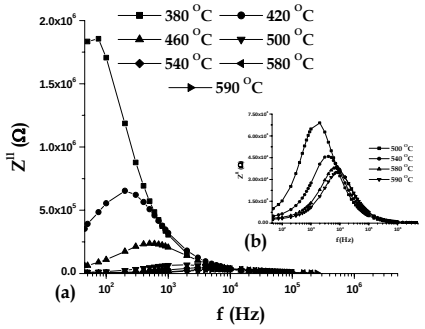

Fig. 10. Variation of imaginary part of impedance (Z") with frequency at different temperatures. Inset: Variation of imaginary part of impedance (500 - 590 °C).

Fig. 9 shows the variation of real part of impedance (Z') with frequency at different temperatures (340 to 590 °C). Also, inset figure shows the same between 80 to 320 °C. It is observed that the magnitude of Z' decreases with the increase in both frequency as well as temperature. The Z' values for all temperatures merge above 10 KHz. This may be due to release of space charge as a result of lowering the barrier properties of the material [32,33]. It has been observed that in low temperature region the magnitude of Z' decreases with the rise in temperature i.e. showing negative temperature coefficient of resistance (NCTR) type behavior as that of semiconductors [34].

Fig. 10 shows the variation of the imaginary part of impedance (Z") with frequency at different temperatures (380 to 590 °C). Inset figure shows the same between 500 to 590 °C. The plots show the Z" values reach a maxima peak ($Z"_{max}$) for temperatures ≥ 380 °C. For the temperatures below 380 °C, the peak was beyond the range of frequency measurement. The value of $Z"_{max}$ shifts to higher frequencies with increase in temperature indicating the increase in loss of the sample. The broadening of the peaks indicates a temperature dependent electrical relaxation phenomenon in the material [35].

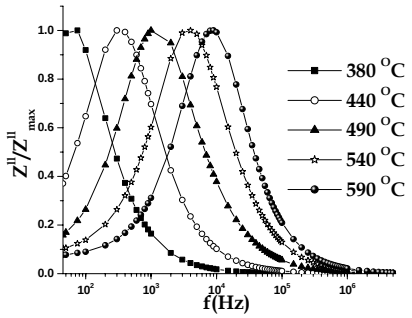

Fig. 11. Normalized part of impedance ($Z"/Z"_{max}$) as a function of frequency at several temperatures.

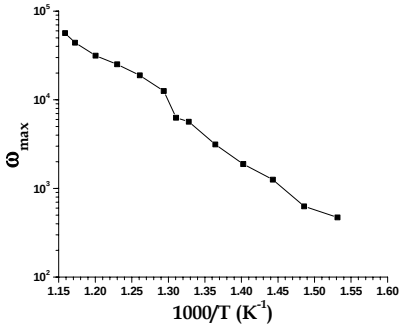

Fig. 12. Temperature dependence of relaxational frequency for PKDN.

Fig. 11 shows the normalized imaginary parts of the impedance ($Z"/Z"_{max}$) as a function of frequency for PKDN at several temperatures. It seems that high temperature triggers another relaxation process, The $Z"/Z"_{max}$ parameter exhibits a peak with a slightly asymmetric degree at each temperature especially at higher temperatures. The asymmetric broadening of peaks suggests the presence of electrical processes in the material with a spread of relaxation time. The relaxation species in the material may possibly be immobile species/electrons at low temperatures and defect/vacancies at higher temperatures. The value of f_{max} shifts to higher side with increase in temperature indicating the increasing loss in the sample.

At the peak, the relaxation is defined by the condition

$$\omega_m \tau_{m=1} \quad (5)$$

Where τ_m is the relaxation time. Fig. 12 shows that the variation of relaxational angular frequency (i.e. frequency at which Z" attains a peak at a particular temperature) with 1000/T follows the Arrhenius law

$$\omega_m = \omega_o \exp(-E_\tau/K_B T) \quad (6)$$

Where ω_o is the pre-exponential factor. The activation energies have been calculated in the temperature regions

380 – 500 ^{O}C and 520 – 590 ^{O}C are 0.49 and 0.43eV respectively.

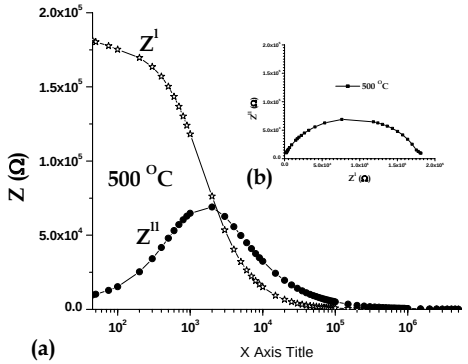

Fig. 13. (a) Frequency dependence of Z' and Z''. (b) Argand diagram.

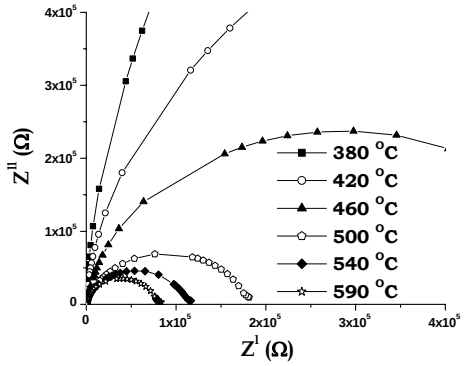

Fig. 14. Complex impedance plots.

Fig. 13 (a) shows the frequency dependence of Z^1 and Z^{11} at 500 ^{O}C. As the frequency increases Z^{11} increases where as Z^1 decreases. This trend continues upto a particular frequency which Z^{11} occupies a maximum value and Z^1 intersects, further increase in frequency both $Z^1$and Z^{11} decreases, and above 10 KHz both the values merges with X-axis. This indicates there exists a relaxation phenomenon [36]. Fig. 13 (b) shows Argand diagram, (imaginary part of Complex impedance Z^* versus its real part) allows the determination of bulk ohmic resistance as a function of temperature and thus temperature dependence of conductivity [37, 38].

Fig. 14 shows the complex impedance plane plot (Cole-Cole) drawn for PKDN at different temperatures. The plot shows a semicircle, starting from origin, making an intercept on the real axis with a large radius. The intercepts of the semicircles with the real axis shifts towards origin and also frequency of the intercept point increases with increase in temperature. The first semi circle corresponds to the grain effects and the second one due to grain boundaries. The center of the semicircles lies below the real axis indicating a non-Debye behavior. The depression in the semicircles below the real axis was presented by an angle θ, which can be related to the width of the relaxation time (τ) distribution. If we consider the semicircle to be made up of a parallel combination of RC elements, using equation $2\pi fRC = 1$, one can calculate the relaxation time (τ), which is the reciprocal of the peak frequency [31]. If the semicircle does not start from the origin, in this case, in addition to the serial combinations of parallel RCs belonging to the grain and grain boundary effects, a series resistance also exists. This kind of effect may have its origin in the structure. We believe that the sample under investigation which is noncentrosymmetric had semicircles starting from origin and have parallel combinations of RC elements connected in series. Complex impedance plot of PKDN at 500 ^{o}C with appropriate equivalent circuit has been shown in Fig. 15.

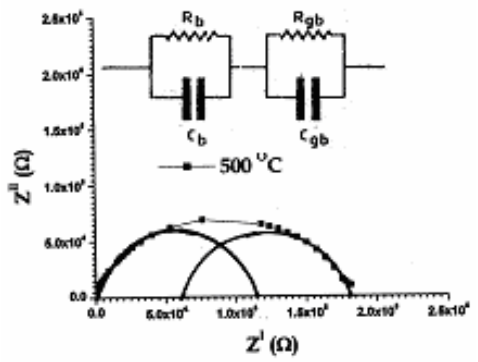

Fig. 15. Complex impedance plot of PKDN at 500 ^{O}C. Inset: Appropriate equivalent circuit.

The resistance of bulk (Rb), grain boundary (Rgb), could directly be obtained from the intercept on the Z'-axis. The capacitance due to these effects can be calculated using

$$f_{max} = 1/(2\pi\tau) = 1/(2\pi RC) \quad (7)$$

The value of R_b, R_{gb}, C_b and C_{gb} at different temperature obtained from the Cole-Cole plots and grain (τ_b) and grain boundary (τ_{gb}) relaxation times at different temperatures are shown in fig. 16 (a) and (b). If the grain and grain boundary resistance and relaxations are plotted against inverse of temperature yields straight lines (Arrhenius plots). Slopes of the lines give the activation energy values of grain (E_b), grain boundary (E_{gb}) of conduction and relaxation (ε_b, ε_{gb}) respectively. These values are given in Table 5.

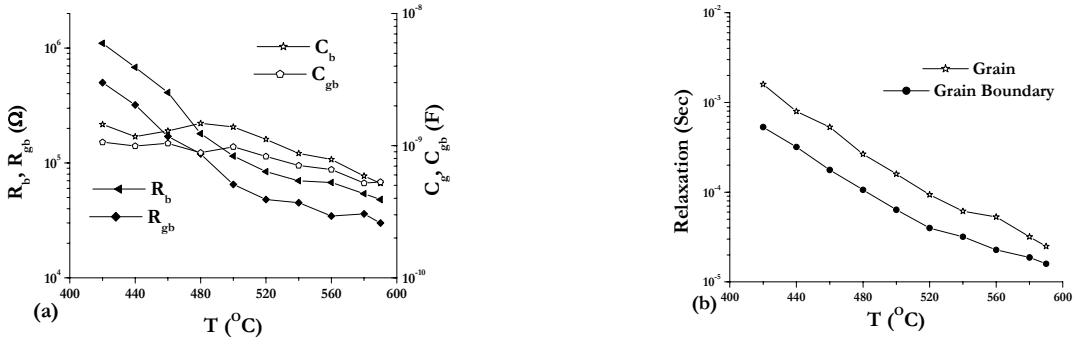

Fig. 16. (a) Variation of R_b, R_{gb}, C_b and C_{gb} with temperature (b) Temperature dependence of bulk and grain boundary relaxation times for PKDN.

Table 5. Activation energy values (eV) for conduction (E) and relaxation (ε) for grain (b) and grain boundary (gb).

Temperature Range (^{O}C)	Grain conduction activation energy, E_b (eV)	Grain boundary conduction activation energy, E_{gb} (eV)	Grain relaxation activation energy, ε_b (eV)	Grain boundary relaxation activation energy, ε_{gb} (eV)
420 - 590	0.35	0.39	0.86	0.79

Electric modulus spectroscopy

Complex modulus, electric modulus or inverse complex permittivity, M*, is defined by the following equation

$$M^* = 1/\varepsilon^* = 1/(\varepsilon' - j\varepsilon'') = \{\varepsilon'/[(\varepsilon')^2+(\varepsilon'')^2]\} + j\{\varepsilon''/[(\varepsilon')^2+(\varepsilon'')^2]\} = M' - jM'' \quad (8)$$

The advantage of adopting complex electric modulus formalism is that it can discriminate against electrode polarization and grain boundary conduction process. It is also suitable in detecting bulk phenomena properties as apparent conductivity relaxation times [31, 39]. In polycrystalline materials, impedance formalism might emphasize the grain boundary conduction process, where bulk effects on the frequency domain would dominate in the electric modulus formalism. The use of a modulus spectroscopy plot is particularly useful for separating components with similar resistance but different capacitance. The other advantage of the electric modulus formalism is that the electrode effect ca be suppressed [40].

Variation of real part of electric modulus (M') with frequency at different temperatures is shown in Fig. 17 (a). At all temperatures, the value of M' reaches at high frequencies, a constant value $M'_\infty(=1/\varepsilon_\infty)$. At low frequencies, it approaches to zero, which indicates the electrode polarization phenomena make a negligible contribution to M* and may be ignored when the electric data are analyzed in this form [41].

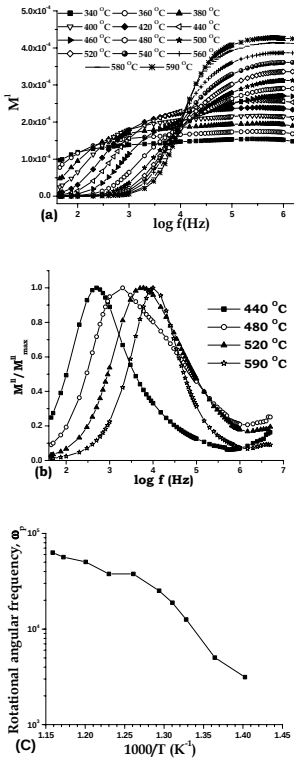

Fig. 17. Variation of (a) real part of electric modulus (M') (b) normalized imaginary part of electric modulus (M''/M''_{max}) with frequency at various temperatures, (c)The Arrhenius plot of relaxational frequency as a function of 1/T for PKDN.

Fig. 17 (b) shows the normalized imaginary part of electric modulus (M"/ $M"_{max}$) with frequency at various temperatures. The $M"/M"_{max}$ spectrum relative to a temperature given shows a asymmetrical peak approximately centered in the dispersion region of M' (Fig. 17 (a)). The region to the left of the peak is where the ions are mobile over long distances; the region to the right is where the ions are spatially confined to their potential wells. The frequency range where the peak occurs is indicative of the transition from long-range to short-range mobility and is defined by the condition $\omega\tau = 1$ where τ is the most probable ion relaxation time [42].

When temperature increases, modulus peak maxima shifts to higher frequencies (Fig. 17 (b)). The temperature dependence of the frequency ($f_p = 1/2\pi\tau$)relative to $M"_{max}$ peak corresponding to the bulk relaxation. An Arrhenius-type law is shown. The activation energy issued from the modulus (ΔE_f) spectra (in the temperature regions 420 – 520 ^{O}C and 540 – 590 ^{O}C are 0.62 and 0.22 eV), suggesting that the ion transport in the material is probably due to a hopping mechanism [43].

AC and DC Conductivity

From the Fig. 6 it can be observed that frequency dependent conductivity show distinct regions, with in the measured frequency range, in which are (a) the low-frequency plateau region and (b) high-frequency dispersion region. The plateau region corresponded to frequency independent conductivity σ (0) or σ_{dc}. The frequency dependent conductivity at various temperatures in the dispersion region was analyzed using JPL [44] $\sigma(\omega) = \sigma(0) + A\omega^s$. The frequency at which the dispersion region diverged from DC conductivity plateau was defined as characteristic frequency ($\omega_p = f_0$) and it be recognized as hopping frequency [45-47]. The relationship between DC conductivity and hopping frequency was given by $\sigma(0) = k\omega_p$, where k is the empirical constant, which depends on the concentration of mobile ions, temperatures and the conduction mechanism [25, 48-49]. The hopping frequency, ω_p at which the relaxation effects begin to appear, moves towards higher frequency with increase in temperature. The frequency dependent conductivity was attributed to the long-range transport of the mobile ions in response to the DC conductivity σ (0).

The behavior of the ac conductivity with temperature for the PKDN sample is shown in Fig. 18. A strong dependence of the conductivity with frequency is observed. The graphs can be divided, independent of frequency, in four temperature regions characterized by different slopes. Every region is characterized by different slopes indicating the presence of different conduction mechanisms associated with their different values of activation energies. The activation energy values have been calculated assuming the Arrhenius behavior and summarized in the table 6 for both ac and dc conductivity.

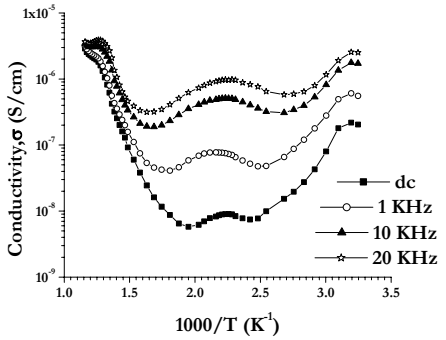

Fig. 18. Variation of Ac and dc conductivity as a function of inverse of temperature.

Table 6. Ac conductivity activation energy values in PKDN.

Composition	PKDN			
Temperature Range (^{O}C)	Ac 20K	10K	1K	dc
40 - 100	0.17	0.20	0.23	0.28
120 - 190	0.056	0.052	0.077	0.043
210 - 270	0.056	0.051	0.068	0.071
320 - 460	0.40	0.28	0.20	0.18

4. Conclusions

Single phase PKDN ceramics have been obtained using the traditional ceramic method. XRD studies show that PKDN exhibits orthorhombic structure. The dielectric data for the present compound is found to fit well to the Jonscher's power law in a fixed range of frequencies and temperatures. The parameters A(T) and n(T) are determined. An anomaly in the paraelectric-ferroelectric transition region is observed for both the parameters near TC indicating a coupling between the charge carriers and the phonons. Impedance analysis indicated the NTCR behavior of PKDN and the presence of grain and grain boundary. The relaxation frequency shifted to higher frequencies with the increase of temperature. Complex impedance analysis suggested the dielectric relaxation to be of polydispersive non-Debye type. Modulus analysis has established the possibility of hopping mechanism for electrical transport process in the system. Frequency dependant ac conductivity at different temperatures indicated that the conduction process is thermally activated process.

References

[1] J. Nakano, T. Ymada, J. Appl. Phys. **46**, 2361 (1975).
[2] T.yamada, J. Appl. Phys. **46**, 2894 (1975).
[3] R. M. O'Connell, J. Appl. Phys. **49**, 3324 (1978).

[4] K. Sambasiva Rao, P. Murali Krishna, T. Swarna Latha, D. Madhava Prasad, Mat. Sci. Eng. B **131**, 127 (2006).
[5] K. Sambasiva Rao, P. Murali Krishna, D. Madhava Prasad, Joon Hyung Lee, Int. J. Mod. Phys. B, In press.
[6] K. Sambasiva Rao, D. Madhava Prasad, P. Murali Krishna, Joon Hyung Lee, Communicated to Mat. Sci. Eng. B.
[7] D. P. Almond, A.R. West, Solid State Ionics **11**, 57 (1983).
[8] C. K. Guo, Y. M. Yan, Solid State Ionics **18/19**, 236 (1986).
[9] Y. T. Tsai, D. H. Whitemore, Solid State Ionics **7**, 129 (1982).
[10] P. B. Macedo, C. T. Moynihan, R. Bose, Phys. Chem. Glasses **13**, 171 (1972).
[11] J. Wong, C. A. Angell, Glass structure by spectroscopy, Marcel Dekker, New York (1976).
[12] P. B. Macedo, R. Bose, V. Provenzano, T. A. Livitz, Amorphous materials, p.251, Wiely, New York (1972).
[13] H. S. Maiti, R. N. Basu, Mat. Res. Bull. **21**, 1107 (1986).
[14] S. K. Sundaram, Ferroelectrics **102**, 129 (1990).
[15] A. Huanosta, A. R. West, J. Appl. Phys. **61**, 5386 (1987).
[16] D. C. Sinclair, A. R. West, Phys. Rev. B, **39**, 13486 (1989).
[17] J. R. MacDonald, Impedance spectroscopy, Wiely, New York, 1987.
[18] Interpretation and Indexing program by E. Wu, School of physical Sciences, Flinders University of South Australia, Bed ford park, Australia.
[19] G. H. Belding, M. G. McLaren, J. Am. ceram. soc. **49**, 1025 (1970).
[20] J. S. Kim, T. K. Song, J. Phys. Soc. Japan, **70**, 3419 (2001).
[21] Sonali Saha, T. P. Sinha, J. Appl. Phys. **99**, 014109 (2006).
[22] Lu Zhigao, J. P. Bonnet, J. Ravez, P. Hagenmuller, Solid State Ionics **57**, 235 (1992).
[23] T. A. Nealon, Ferroelectrics **76**, 377 (1987).
[24] A. K. Jonscher, R. M. Hill, C. Pickup, J. Mater.Sci. **20**, 4431 (1985).
[25] B. Roling, A. Happe, K. Funke, M. D. Ingram, Phy. Rev. Lett. **78**, 2160 (1997).
[26] W. K. Lee, J. F. Liu, A. S. Nowick, Phy. Rev. Lett. **67**, 1559 (1991).
[27] Z. Lu, J. P. Bonnet, J. Ravez, P. Hagenmuller, Eur. J. Solid State Inorg. Chem **27**(2), 363 (1991).
[28] A. K. Jonscer, Dielectric relaxation in solids, Chelsea Dielectric press, London, 1983.
[29] K. Sambasiva Rao, T. N. V. K. V. Prasad, A. S. V. Subrahmanyam, J. H. Lee, J. J. Kim, S. H. Cho, Mater. Sci. Eng. B, **98**, 279 (2003).
[30] R. R. Neurgoanker, J. R. Oliver, J. G. Nelson, L. E. Cross, Mater. Res. Bull. **26**, 771 (1991).
[31] D. C. Sinclair, A. R. West, J. Appl. Phys. **66**, 3850 (1989).
[32] J. Maier, J. Eur. Cer. Soc. **24**, 1343 (2004); Prog. Solid state Chem. **23**, 171 (1995).
[33] Idem., Solid State ionics **157**, 327 (2003); **154/155**, 291 (2002); **148**, 367 (2002).
[34] D. K. Pradhan, B. K. Samantaray, R. N. P. Choudhary, A. K. Thakur, J. Mat. Sci. **40**, 5419 (2005).
[35] A. K. Jonscher, Nature **267**, 673 (1977).
[36] V. Hornebecq, J. M. Reau, J. Ravez, Solid State Ionics, **127**, 231 (2000).
[37] K. S. Cole, R. H. Cole, J. Chem. Phys. **9**, 341 (1941).
[38] J. E. Bauerle, J. Phys. Chem. Solids **30**, 2657 (1969).
[39] I. M. Hodge, M. D. Ingram, A. R. West, J. Electronal. Chem. Interfacial Electrochem. **74**, 125 (1976).
[40] S. Sen, P. Pramanik, R. N. P. Choudhary, Appl. Phys. A, **82**, 549 (2006).
[41] F. S. Howell, R. Bose, P. B. Macedo, C. T. Moynihan, J. Phys. Chem. **78**, 639 (1974).
[42] L. M. Hodge, M. D. Ingram, A. R. West, J. Electronal. Chem. **74**, 125 (1976).
[43] B. V. R. Chowdari, R. Gopalakrishnan, Solid State Ionics **23**. 225 (1987).
[44] A. K. Jonscher, J. Mater. Sci. **16**[8], 2037 (1981).
[45] D. L. Sidebottom, P. F. Green, R. K. Brow, Phy. Rev. B **56**(1), 170 (1997).
[46] M. D. Ingram, Phys. Chem. Glasses, **28**(6), 217 (1987).
[47] H. Jain, J. N. Mundy, Solid State Ionics, **91**(3-4) (1997).
[48] A. H. Verhoef, H. W. den Hartog, Solid State Ionics, **68**(3-4), 315 (1994).
[49] H. K. Patel, S. W. Martin, Phys. Rev. B, **45**(18), 10292 (1992).

*Corresponding author: konapala@sify.com, konapala@hotmail.com